SAND2019-14589C

Inverse Methods for Identifying Pressure Loading on Aerospace Vehicles using Structural Response

Peter B. Coffin* and Carlie Dennard† and Julie Pham‡
Sandia National Laboratories, Albuquerque, NM 87185

Accelerometers are commonly installed on aerospace vehicles to monitor structural response. Robust ways of identifying the fluid pressure loading associated with those measurements would be useful in understanding the fundamental environments the vehicle is being exposed to during operation. A study is performed to compare multiple inverse methods for their applicability to identify fluid pressure loading of a slender conical structure subject to hypersonic flow in a wind tunnel. The wind tunnel experiment consists of a structure with an instrumented, thin, flexible panel that was excited by the turbulent boundary layer. The turbulent loading was measured using multiple types of pressure sensors. To limit the number of unknowns and ensure a well-posed problem, the first inverse method demonstrated consists of a random vibration analysis computed in the frequency domain and subject to a parameterized pressure distribution. The second approach is a generic force identification of pressures in the time domain. In the study, the influence of the methods on the characteristics of the identified pressures are discussed as well as the computational costs and implementational considerations.

I. Nomenclature

η	=	correlation length scale in streamwise direction
H_ω	=	transfer function at frequency ω
N_c	=	finite element interpolation of coarse grid nodes to original finite element nodes
N_p	=	application of nodal pressures to nodal forces
S_F	=	spectral density of nodal forces
S_P	=	spectral density of pressure
S_X	=	spectral response of model
ω	=	circular frequency
p_c	=	pressures on coarse grid nodes
p_f	=	pressures on original finite element mesh nodes
ψ	=	magnitudes of log-linear interpolation functions
Ψ	=	autocorrelation function
Ψ_F	=	log-linear interpolation function in frequency
Ψ_S	=	linear interpolation function in space
r	=	radius in cylindrical coordinate system
ρ	=	correlation length parameter for spanwise direction
θ	=	angle in cylindrical coordinate system
u	=	free-stream flow velocity
x	=	axial coordinates
ζ	=	spanwise distance
Z	=	objective function

*Senior Member of the Technical Staff, Engineering Sciences Center, Member AIAA, pcoffin@sandia.gov, (505) 845-8798.
†RAMS Institute Intern, Engineering Sciences Center, cdennar@sandia.gov.
‡RAMS Institute Intern, Engineering Sciences Center, jvpham@sandia.gov.

Sandia National Laboratories is a multimission laboratory managed and operated by National Technology & Engineering Solutions of Sandia, LLC, a wholly owned subsidiary of Honeywell International Inc., for the U.S. Department of Energy's National Nuclear Security Administration under contract DE-NA0003525.

II. Introduction

Quantities of interest are frequently not measurable in field environments for many different disciplines. For aerospace vehicles, the varying surface pressure resulting from the turbulent boundary layer can be a primary cause of structural vibration, and in this work, is the environment of interest. Characterizing these pressures is necessary to understand flight environments; however, direct measurement of these pressures during operation or testing is much less common than sparse measurement of the resulting structural vibration. Common pressure measurement paradigms require holes in the exterior surface of the body that may impact performance or integrity of the vehicle. Instead, accelerometers are used because they are small, lightweight and can be placed internal to the vehicle, thus not significantly impacting the integrity of the body. In this work, two inverse methods are studied in an attempt to utilize detailed structural models of the vehicle combined with measurements of structural response to identify the pressure loading experienced by a vehicle.

Inverse problems are those in which the unknown quantity is characterized as the cause and the known quantity is the effect. In this case, the load is unknown, typically the input to a simulation and the response (acceleration) is known. The inverse methods used here will be described in the context of optimization as both are fundamentally optimization problems, optimizing the parameters of some unknown load to yield the best match to the measured acceleration. A variety of source or load identification inverse problems exist and have been demonstrated in literature. Problems such as earthquake localization [1][2], defect identification [3][4], acoustics [5][6], vibroacoustics for medical imaging [7], volcanic eruption characterization [8] have been solved with a variety of techniques. These problems are well known to be problematic due to noisy data and non-unique solutions [9][10].

A model for the pressure loading resulting from the hypersonic turbulent boundary layer has been studied, compared to experiment [11] and has significant historical context going back at least 50 years [12]. This model has complex dependency on a number of parameters that may not be well known for a given test and so it is still desirable to be able to work backward from the structural response to identify the correct pressure parameters; this allows comparison to the expected values, continued validation of the Turbulent Boundary Layer (TBL) pressure loading model and identification of situations where the TBL may not be the primary loading phenomena. Given these motivations two different approaches are studied. First, a frequency domain representation where much of the existing model from Smith et al. [11] is assumed and only a few parameters and scalings of the model are fit. This addresses the problem of uniqueness by only fitting the minimum number of parameters necessary. Second, a time domain representation using Sierra/SD [10] where little is assumed about the form of the loading and typical L2-norm Tikhonov regularization is used to address the non-uniqueness.

The frequency domain inverse method will be discussed in detail in Section V while the time domain approach will be discussed in Section VI. Both methods are applied to synthetic problems using the same finite element model and representative pressure loads to demonstrate characteristics of the approaches. Then the methods are each applied to the actual wind tunnel experimental data. A discussion comparing the methods and their pressure predictions will be shown in Section VII. The two approaches will be demonstrated and compared using data recorded during a wind tunnel experiment consisting of a slender cone with flexible panel subject to hypersonic flow and will be discussed in III.

III. Experimental Setup

The experiment used in this work was developed to understand the fluid-structure interaction of conical bodies in hypersonic flow. The experimental setup consists of a 7° half angle cone mounted in the Sandia Hypersonic Wind Tunnel, shown in Figure 1. The cone features a thin, flexible, carbon-composite panel near the rear of the body that is designed to be well-excited by the flow. Accelerometers were mounted on the panel and on the cone body to measure the response during testing. Pressure transducers were also mounted at various locations on the model to measure the actual fluid pressure loading on the surface near the panel. Details of this experiment can be found in work by Casper et al. [13]. The cone and panel were subject to Mach 8, Re= 13.7×10^6 /m flow.

IV. Finite Element Model Development

A. Overview

A finite element (FE) model was constructed and calibrated using a modal hammer test. The hammer test utilizes an instrumented hammer to excite the structure at various locations while additional accelerometers are present. The data

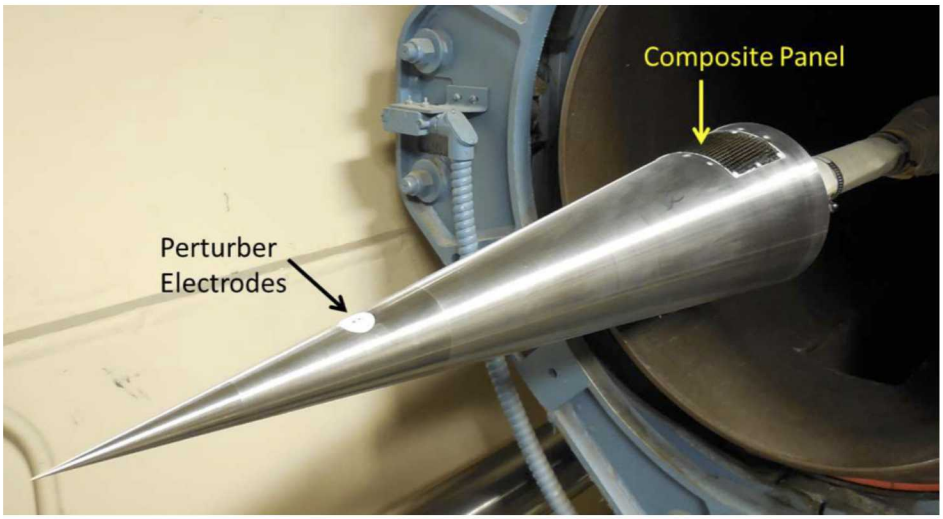

Fig. 1 HWT Cone in wind tunnel.

from this can be used to identify structural modes that are then compared to the FE model and used to update properties as necessary to calibrate the model. The FE model is a hexahedral dominated mesh with some wedge elements and approximately 600k nodes. Figure 3 shows a cross section of the panel in the model, with at least 6 elements through the thickness.

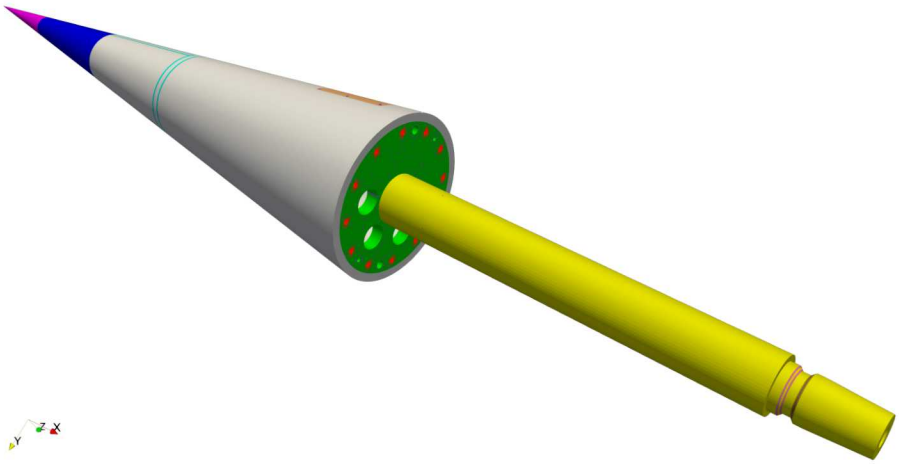

Fig. 2 HWT Cone Finite Element Model.

The experimental data used in this report was measured in the coordinate system in Figure 4, local to each measurement location.

B. Measurement Locations

Five accelerometers were utilized during the wind tunnel tests. One triaxial accelerometer (G1) was located in the center of the plate. Three single axis accelerometers (G3, G4, G5) were located at mid-panel locations upstream, downstream and to the side of the mass mount. A final triaxial accelerometer (G2) was mounted near the sting attachment point. Figure 5 depicts these locations.

Fig. 3 Cross-section of composite panel in Finite Element Model, showing number of elements in thickness.

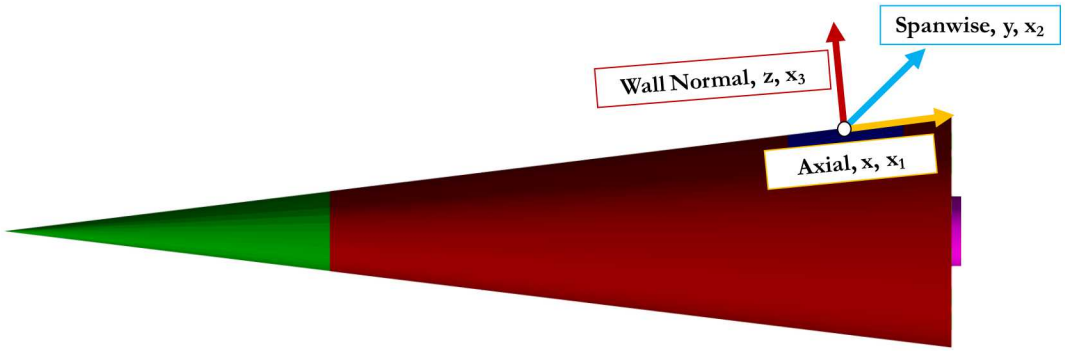

Fig. 4 Coordinate system used in the experimental measurements as well as the calculations presented in this report.

C. Boundary conditions

The original FE model was constructed with part of the sting and mounting apparatus included, as seen in Figure 2. In the wind tunnel the sting is attached to additional structure that results in a relatively long, flexible, cantilever beam. Studies were performed to understand the motion of the cone on sting during operation as it dominate the response for certain configurations and frequencies. Good agreement with the model was found when the three translations measured by G2 were prescribed on the model at the cross-section of the sting near the body. For frequency domain analyses the assumption was made that this motion and its corresponding loads were uncorrelated with the pressures on the surface of the body. For time domain analyses (Section VI.B.2) the time history of motion was applied to the model and no assumptions about its relation to the identified pressures were enforced.

D. Discretization of TBL Pressures

For the purposes of computational cost the definition of pressures due to the TBL are not prescribed node-by-node or on individual element faces on the surface of the body. Different approaches are used to define a coarser representation of the pressure for the time and frequency domain analyses, via collections of element faces, denoted here as patches and by interpolation of a coarser grid of nodes to the nodes on the surface, respectively. The reasons for two different schemes are historical and either representation could be used for either analysis.

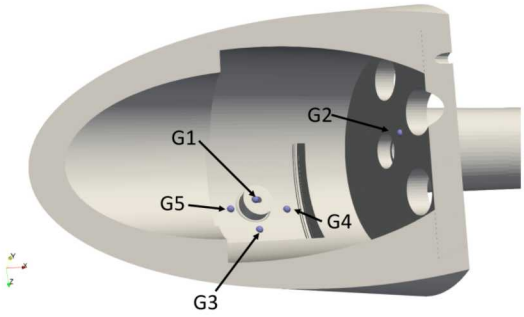

Fig. 5 Accelerometer locations for composite panel with no additional mass, Mach 8.

In the time domain the element faces on the surface of the body are arranged with nearby neighbors into patches in a quilt-like pattern. The patch representation is used to construct a piecewise constant discretization. In the frequency domain a coarser, cylindrical grid is defined over the cone. Bi-linear (in the cylindrical axial and radial coordinates) are used to interpolate from pressures defined on the coarse nodes to the original, fine FE mesh on the cone.

V. Frequency Domain Approach

A. Analysis Framework

MATLAB® was chosen as the environment to demonstrate this approach due to: existing tools for working with finite element model data and the simplicity in performing mathematical operations. An object-oriented framework was constructed to perform necessary FE model functions. The modal solution computed in Sierra/SD was read into the MATLAB® routines and then used to construct the necessary transfer functions and loadings. The standard MATLAB® optimization function `fmincon` was used for simplicity.

B. Objective Function

One objective function has been the focus of the work to date. It is strongly encouraged that more alternative objective functions be investigated in future work. The objective function Z used here is written as:

$$Z = \sum_k \left(\sum_i \left\{ \sum_j \left[\ln(S_{X,ij}(\omega_k) - \ln(\tilde{S}_{X,ij}(\omega_k)) \right]^2 \right\} \right), \tag{1}$$

where $S_{X,ij}(\omega_k)$ is the spectral density of the acceleration of degree of freedom (DOF) i with respect to DOF j at the k-th frequency, ω_k and $\tilde{S}_{X,ij}(\omega_k)$ is the spectral density of the acceleration of DOF i with respect to DOF j at the k-th frequency, ω_k as measured in the experiment.

Two alternative objectives were considered and a comparison will be discussed in Section V.E.2. First, the Frobenius Norm (written later as FNorm):

$$Z = \sum_k \left(\sum_i \left\{ \sum_j \left[(S_{X,ij}(\omega_k) - (\tilde{S}_{X,ij}(\omega_k)) \right]^2 \right\} \right), \tag{2}$$

and secondly, the log of the Frobenius Norm (logFNorm):

$$Z = \ln \left(\sum_k \left(\sum_i \left\{ \sum_j \left[(S_{X,ij}(\omega_k) - (\tilde{S}_{X,ij}(\omega_k)) \right]^2 \right\} \right) \right). \tag{3}$$

C. Response Calculation

The calculation of the model spectral response, S_X, is computed from the spectral density of nodal forces, S_F, as:

$$[S_X] = [H(\omega)]\,[S_F]\,[H(\omega)]^*, \tag{4}$$

where $H(\omega)$ is the transfer function at frequency ω and $[H(\omega)]^*$ is the conjugate transpose of that [14].

D. Turbulent Boundary Layer Pressure Load Parameterization

The target load parameterization was developed to retain the Corcos-like [12] spatial correlation but allow for a free description of the autocorrelation. The spectral density of pressure, S_{P12}, at point 1 with respect to point 2 is defined as:

$$S_{P12}(x_1, x_2, \zeta_{1,2}, \omega) = \sqrt{\Psi(x_1, \omega)\Psi(x_2, \omega)}\; e^{-\frac{i\omega}{u}|x_2 - x_1|}\; e^{-\frac{\eta\omega}{u}|x_2 - x_1|}\; e^{-\frac{\rho\omega}{u}\left|\zeta_{1,2}(\theta_1, \theta_2, r_1, r_2)\right|}. \tag{5}$$

Here x_1, x_2 are the axial coordinates for the two points. $\zeta_{1,2}(\theta_1, \theta_2, r_1, r_2)$ is the spanwise distance between points 1 and 2, a function of θ_1, θ_2, the angle to the points in a cylindrical coordinate system, and r_1, r_2, the radii in that coordinate system. The free-stream flow velocity is u, η is a parameter defining spatial correlation length scales in the streamwise direction and ρ is the parameter for the spanwise direction. $\Psi(x_i, \omega)$ is the autocorrelation of the i-th point at frequency ω, defined as:

$$\Psi(x_i, \omega) = \Psi_S(x_i, \tilde{\mathbf{x}}, \psi_\mathbf{S}) \cdot \Psi_F(\omega, \tilde{\omega}, \psi_\mathbf{F}), \tag{6}$$

where $\Psi_S(x_i, \mathbf{x}, \psi_\mathbf{S})$ is a linear interpolation function where the base axial coordinates are $\tilde{\mathbf{x}}$ and magnitudes are $\psi_\mathbf{S}$. $\Psi_F(\omega, \tilde{\omega}, \psi_\mathbf{F})$ is a log-linear interpolation function in frequency where the base frequencies are $\tilde{\omega}$ and the magnitudes are $\psi_\mathbf{F}$.

Early work with this approach computed the spectral density of pressure nodally, that is S_{P12} of every node on the exterior with respect to every other node. With inspection it is clear that for the lower frequencies of interest the model produced strong correlation across the entire length of the mesh, making the math expensive in the current setting. For higher frequencies, the matrix would become more sparse. These characteristics lead to the use of a coarser representation of the pressures. For the greatest flexibility and efficiency, while retaining accuracy across frequency ranges, it may be desirable in future development to allow for different pressure discretizations at different frequencies. To coarsen the pressure discretization, a Cartesian grid was overlayed in a cylindrical coordinate system and then mapped to the surface of the fine original FE mesh. In the axial and angular axes of the cylindrical coordinate system, the interpolation functions from the coarse grid to the fine grid were computed so that the following could be written:

$$\{p_f\} = [N_c]\{p_c\}, \tag{7}$$

where the pressures on the fine grid nodes, p_f, are a linear interpolation (N_c) of the pressures on the coarse grid nodes p_c. Given that the nodal forces (f_p) from pressures on the fine (FE) grid is written as:

$$\{f_p\} = [N_p]\{p_f\}. \tag{8}$$

Then the spectral density of nodal forces can be written as:

$$[S_F] = [N_p][N_c][S_{P,coarse}][N_c]^T[N_p]^T, \tag{9}$$

where the spectral density matrix of forces on DOFs, S_F, is a function of the spectral density of pressures at nodes on the coarse grid $S_{P,coarse}$.

E. Results

1. Overview

In the results shown, the autospectrum interpolation values $\psi_\mathbf{F}$ were fitted and the values of ρ and η will be prescribed. A number of interpolation frequencies were evenly distributed across the frequency range that will be fitted, from 1kHz to 10kHz. $\psi_\mathbf{F}$ is constrained to be between 1×10^{-10} and 1×10^{14}. The value of ρ is 0.36 and η is 0.7, correlation length scales that have been estimated from wind tunnel data in previous work. The axial variation of the autospectrum $\psi_\mathbf{S}$ was set to be constant values of 1.0.

2. Comparison to Synthetic Example

A synthetic inverse problem is first used to provide a simplified view of the impact of the coarse grid resolution and the objective function definition. Here the FE model is subjected to time-domain patch pressures that are constructed to simulate a TBL environment. Figure 6 shows the autospectrum of acceleration response that results from using the

three different objective functions discussed in Section V.B. It is clear, when considering the autospectrum alone, a logarithmic scaling of the objective is beneficial. The natural log of the Frobenius norm and the original objective both appear to behave similarly with the original objective yielding a better match at low frequencies and the natural log of the Frobenius norm performing better at higher frequencies.

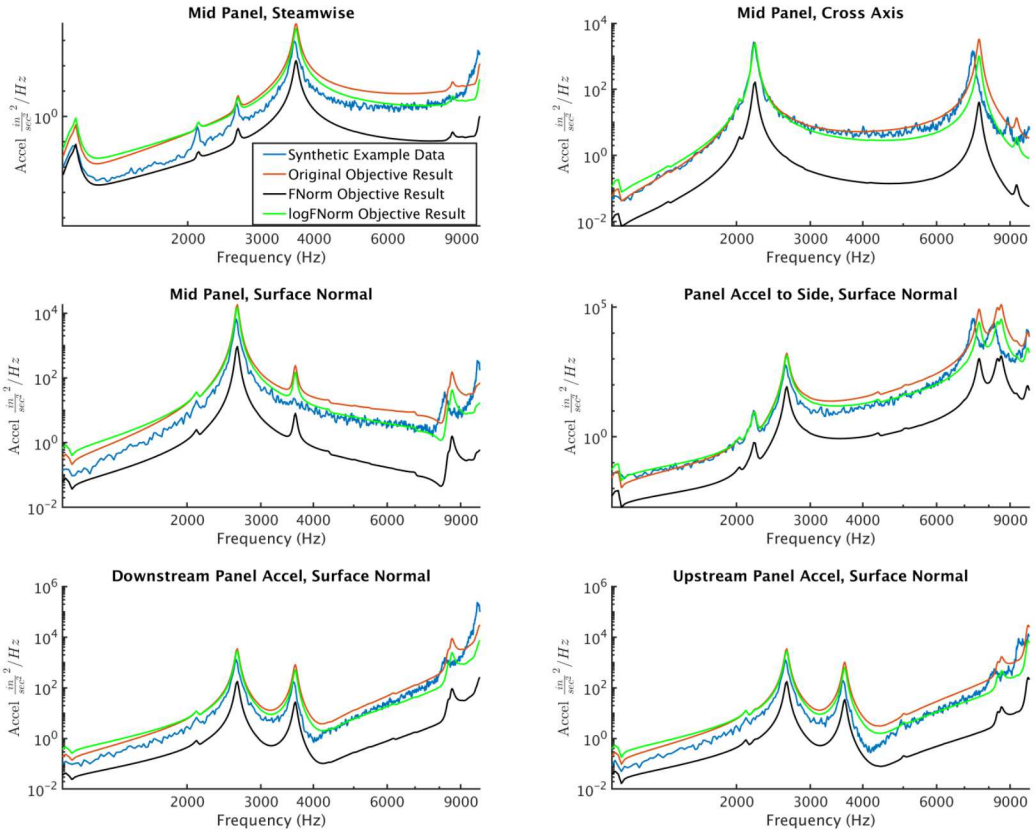

Fig. 6 Response of fitted load parameters to synthetic example using different objective functions.

Figure 7 shows the predicted pressure autospectrums when solving with different coarse grid refinements. The interval is used in the axial direction and an interval in the circumferential direction is computed so that at each refinement the aspect ratio of elements is roughly unity. From the synthetic example it appears that a coarse grid interval of 20 or 30 would represent a good balance of accuracy and computational cost. The cost per objective evaluations (including forward model run) are shown in Table 1. These times were generated on a workstation with an Intel® Xeon® E5-2670 CPU with 8 cores and 16 total threads running Red Hat® Linux and MATLAB® R2018b. Most of the computational time was spent computing $S_{P,coarse}$ and its partial derivatives. The calculation was decomposed into parts that were frequency dependent and those that were independent to avoid unnecessary, repeated calculations. In testing it was found that utilizing parallel `for` loops did not provide any significant gains beyond use of the MATLAB® threaded matrix math operations.

3. Wind Tunnel Data Match

Figure 8 shows the response predictions after fitting the TBL pressure model frequency autospectrum when accounting for sting motion. The sting motion was incorporated by adding the response solely due to the sting motion to the response resulting from the TBL pressure loading. This procedure assumes that the motions are uncorrelated. Figure 9 shows the fitted pressure autospectrum compared to a pressure model that was calibrated using the wind tunnel

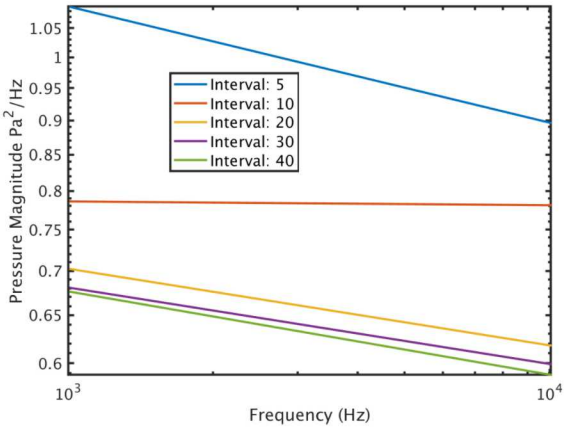

Fig. 7 Predicted pressure autospectrum using different coarse grid refinements for a synthetic example.

Table 1 Frequency Domain Computational Cost.

Interval Size	Single Objective Evaluation Time (min)	Total Optimization Time (hr)	Relative Objective Drop	Absolute Final Objective Value
5	0.56	0.247	0.0527	1.695×10^5
10	1.01	0.345	0.0489	1.615×10^5
20	8.65	1.918	0.0462	1.566×10^5
30	38.77	7.868	0.0457	1.557×10^5
40	126.79	26.61	0.0456	1.557×10^5

pressure measurements. The fit with sting motion was performed using eight interpolation points. In Figure 8 there is little visual difference in the resulting response autospectrum resulting from the different coarse grid intervals. The primary differences are seen above 3kHz and particularly, on the Mid Panel (G2) cross Axis response.

Figure 10 compares response from inverse problems where the pressure autospectrum is either solely dependent on the axial coordinate or solely dependent on the frequency. Both used a coarse grid interval of 20. It is not clear from Figure 10 that either does a significantly better job at matching the response. The final absolute objective value for the axial variation, 1.619×10^5, is larger than that of the frequency only variation, 1.42×10^5. The variation of pressure autospectrum with axial coordinate is shown in Figure 11.

VI. Time Domain Approach

A. Method

Sierra/SD has a time domain, force identification capability that is used[15]. No random vibration (multi-input) frequency domain capability exists similar to that used in Section V so the time domain force identification capability represents the most promising off-the-shelf solution for identifying pressure loading in the Sierra suite. This capability uses a time domain finite element simulation to compute responses at a number of points. The L2-norm of the difference between these responses and the desired (measured) responses is used as the objective for an optimization problem that is solved using the Rapid Optimization Library (ROL). Either a direct or modal method may be used for the forward analysis. The modal method was used in an effort to yield the most computationally efficient solution, particularly due to the complexity of the finite element model and large number of time steps necessary to resolve the frequency range of interest.

Sierra/SD will invert for a set of time dependent pressures in this approach. These time dependent pressures are

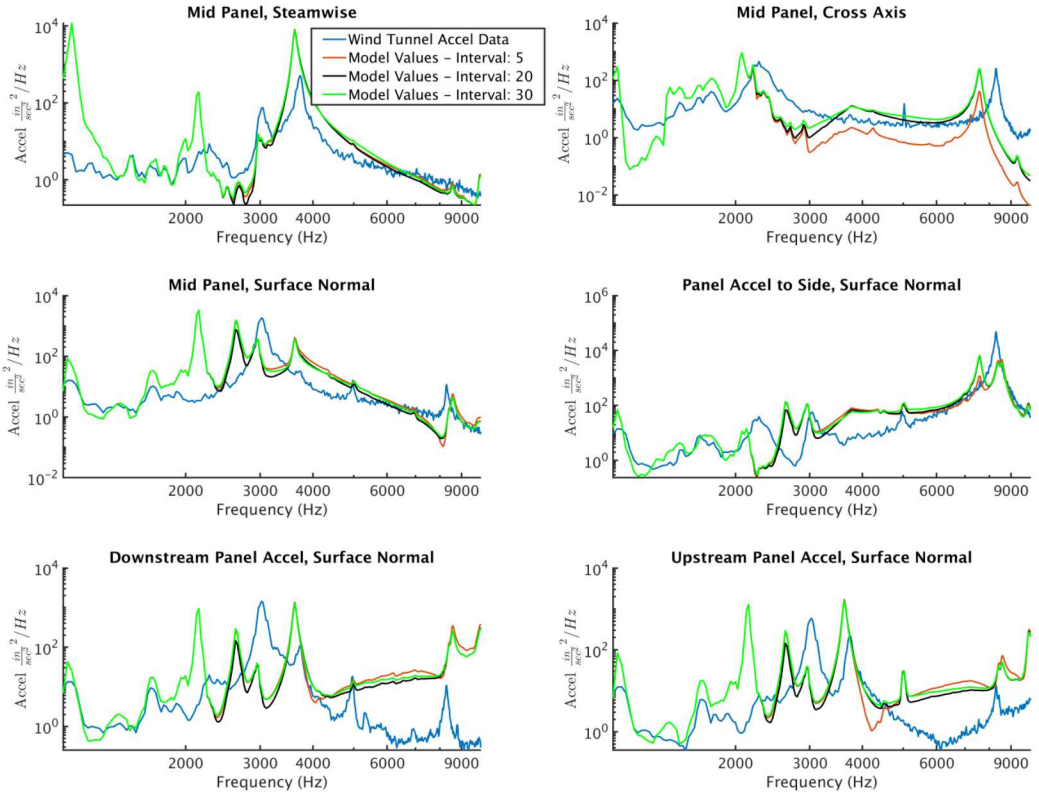

Fig. 8 Response of fitted frequency dependent pressure autospectrum to experiment with varying coarse grid size.

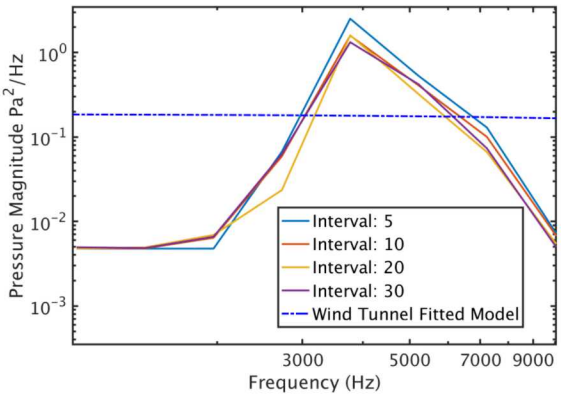

Fig. 9 Comparison of fitted pressure autospectrum with various coarse grid intervals to experiment.

defined as independent and acting individually on patches. Patches are simply groups of element faces on the exterior of the body. An important choice is the number and relative sizing of the patches used. Only one patch could be defined: one pressure acting on the entire outside of the body, or as many patches as there are elements on the outside of the body such that each exterior element has its own unique pressure applied to it. In this work rectangular patches will be defined

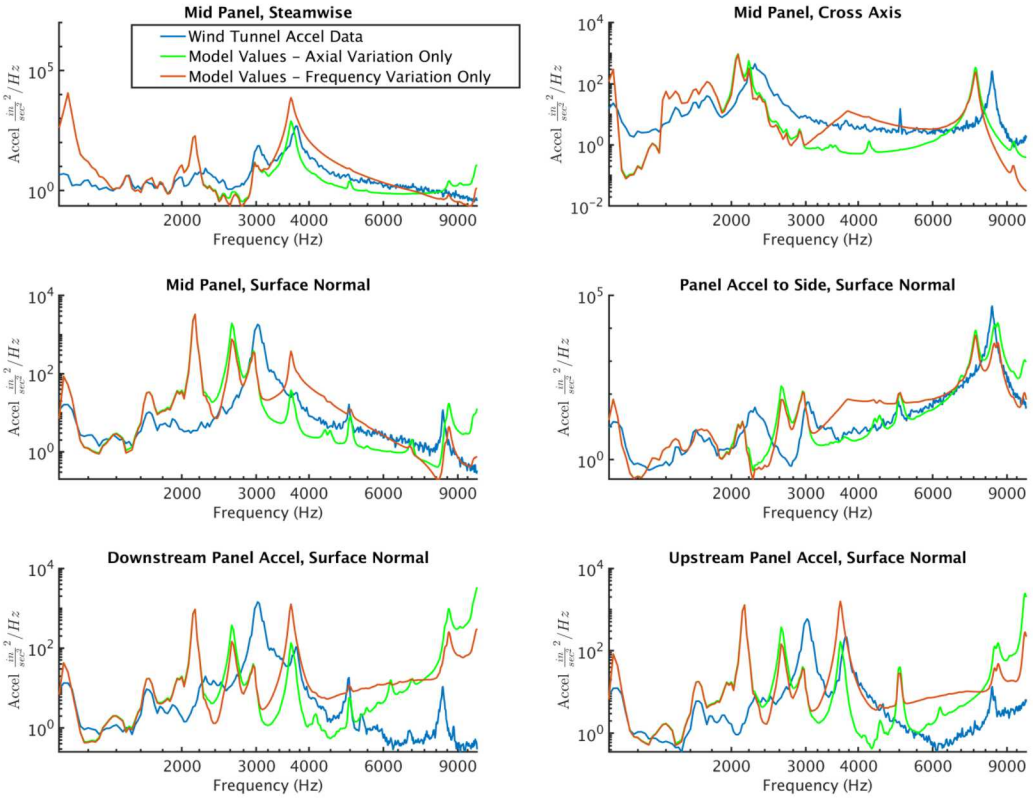

Fig. 10 Response of fitted axial coordinate dependent pressure autospectrum to experiment with varying coarse grid size.

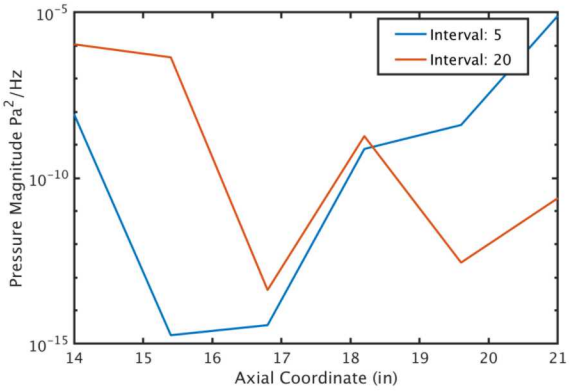

Fig. 11 Comparison of fitted pressure autospectrum variation with axial coordinate.

by the number in the axial direction along the body and in the circumferential direction. Given the limited number of measurements it is expected that the optimization should be well posed when there are few patches on the body but poorly posed when there are many patches on the body. The precise implications of this are of primary interest in this work. Existing knowledge of the turbulent boundary layer pressures implies that for higher frequencies of interest, many patches may be needed on the body to well represent the loading.

To regularize poorly posed optimization problems Sierra/SD provides Tikhonov regularization. Tikhonov regularization is simply an additional term in the objective function that is the L2-norm of the pressure time histories. The relative scaling of this term is expected from earlier demonstrations to have a significant impact on the convergence of the optimization problem and the resulting pressure predictions. In this work the impact will be characterized.

B. Results

The Sierra/SD time domain inverse method will be applied to two demonstration problems using the HWT cone model: a simplified synthetic example where the responses are constructed using the FE model and a set of representative patch pressures, and secondly, the identification of pressures that best replicate the responses measured during the wind tunnel test. For the time domain method a time step of 4×10^{-5} sec was selected and 1000 time steps were solved. These values were chosen to achieve resolution between 1 and 4 kHz while balancing signal processing considerations and computational effort.

1. Synthetic Example

In this example a set of representative pressure realizations were first applied to a subset of patches that lie on the panel, shown in Figure 12. This generated a set of displacement responses, in all three coordinate directions, on each of the accelerometer locations on the panel (G1, G3, G4, and G5). The number of loaded patches was selected to be equal to the number of measurement degrees of freedom (12). The inverse problem was then solved for a selection of Tikhonov regularization scalings to understand the impact of the regularization on the resulting pressures and responses. The

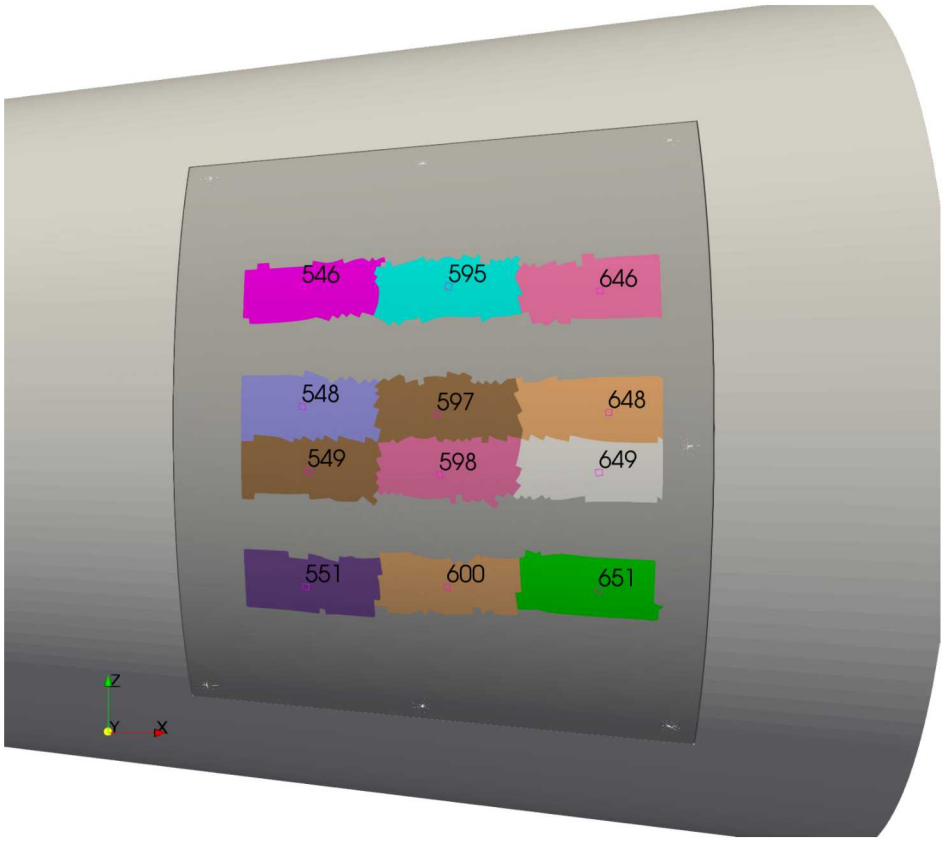

Fig. 12 Patches selected for loading in synthetic example with identifying numbers.

inverse problem was solved using a Newton-Krylov method, limited to 5000 Krylov iterations and 4 total optimization iterations. The relative objective and gradient tolerance were 1×10^{-8}. These parameters were chosen to provide the most accurate solution to the problem while still ensuring that the method would cease within an acceptable amount of computational time. Figure 13 shows the relationship between the final response error and the prescribed Tikhonov

scaling parameter. For scalings smaller than 10^{-6}, the method achieves the prescribed objective tolerance of 10^{-8} for the response match.

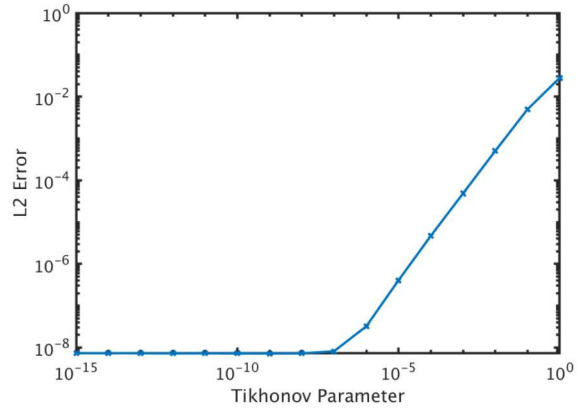

Fig. 13 Error in response match as a function of Tikhonov scaling.

Figure 14 shows the relationship between the number of Krylov iterations used by the solver and the Tikhonov scaling. A Tikhonov scaling of 10^{-3} is the smallest value that results in fewer than the maximum number of iterations used. This indicates that the problem remains poorly conditioned and difficult for the optimization methods in Sierra/SD to solve for scalings smaller than 10^{-3}. No preconditioner currently is utilized by these methods and this may be an indication that preconditioning would beneficial for this and similar load identification problems.

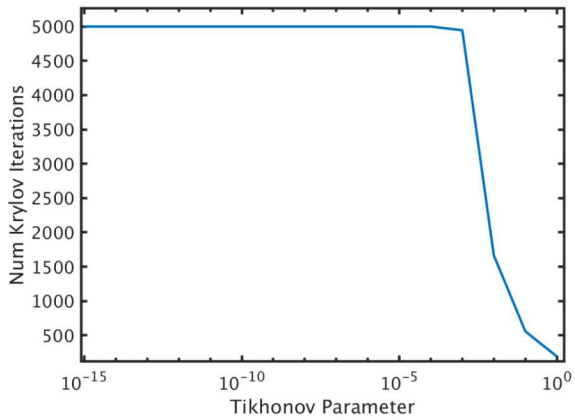

Fig. 14 Number of Krylov iterations used with varying Tikhonov scaling.

Figures 15 and 16 show the autospectrum of the magnitude of displacement response at two locations for various Tikhonov scalings. The responses at other locations were visually similar to Figures 15 and 16. In these figures the response from the original forward solution and those resulting from scalings less than 10^{-3} are visually identical. Additionally, for the peaks around modes' resonances the results are indistinguishable even for larger scaling values. It is in the anti-resonances that significant differences occur for large scaling values.

Figures 17 and 18 show the autospectrum of the predicted pressure loads for various Tikhonov scalings. These two patches demonstrate the two different trends that are observed when studying the predicted pressure across all patches, either strong frequency dependence of the agreement or little dependence on frequency. In Figure 17, the agreement between patch pressures and the original load has little dependence on the frequency, conversely, Figure 18 shows that as the scaling decreases, the frequency range of good agreement increases. In both figures it appears that a scaling less than 10^{-5} is necessary to achieve a visually similar pressure to the original load.

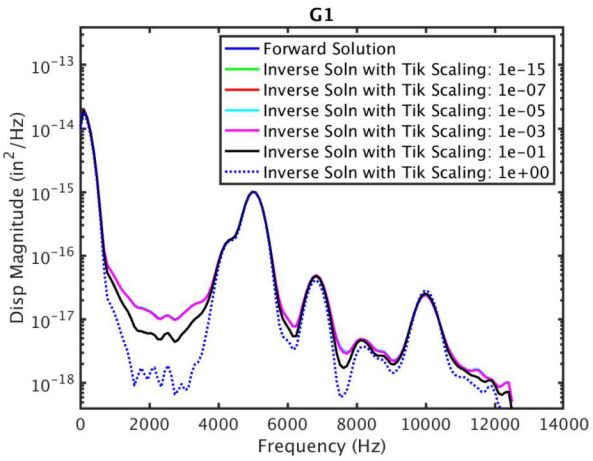

Fig. 15 Response at G1 with varying Tikhonov scaling.

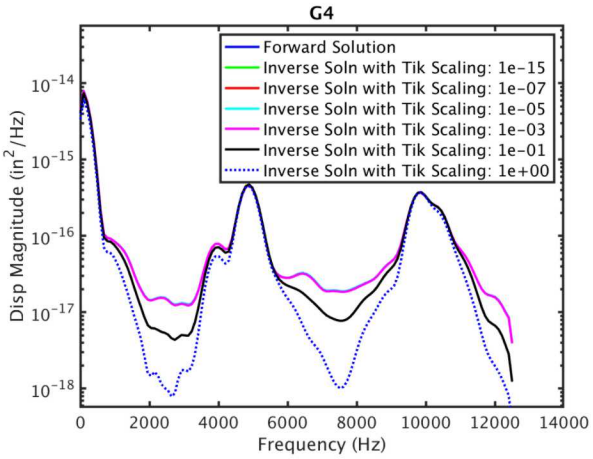

Fig. 16 Response at G4 with varying Tikhonov scaling.

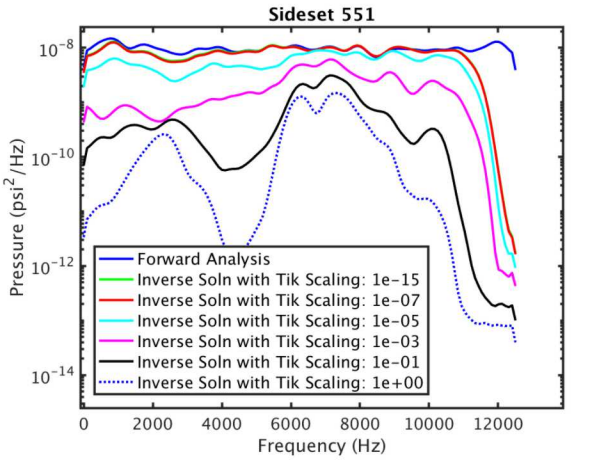

Fig. 17 Predicted pressure loads on patch 551 with varying Tikhonov scaling.

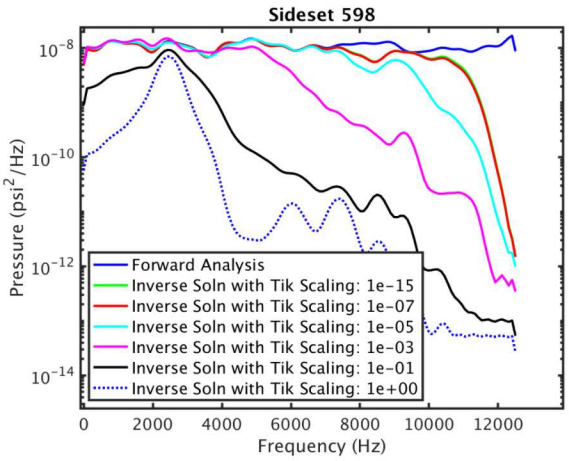

Fig. 18 Predicted pressure loads on patch 598 with varying Tikhonov scaling.

2. Wind Tunnel Load Identification

In this section, the results when performing the inverse problem to identify the wind tunnel pressure loads are presented. Comparisons are first shown where the inverse problem only includes accelerometers G1, G4 and G5, to avoid alignment issues with G3. Currently Sierra/SD requires the inverse problem data to be prescribed in model global coordinates, which for this model can be transformed to align with G1, G2, G4 and G5, but not precisely with G3. The boundary condition at the sting is fixed in initial comparisons. Figure 19 shows the response resulting from the inverse problem at panel accelerometers when varying Tikhonov scalings are used. A mesh with 45 patches is used. For scalings less than 10^{-3} the overall match is visually good, with smaller scalings having better agreement in certain frequency ranges and measurement DOFs. The mean patch pressures predicted by these inverse problems are shown in Figure 20. Between the smallest and largest scalings there is a one to two order of magnitude difference in the pressure autospectrum and the offset is relatively constant across frequency. If the mean patch pressure of only the patches on the panel (50% or more of element faces on panel) are plotted, Figure 21, the pressure is larger and the offset varies more significantly with frequency. Subsequent plots in this section will only show the mean of pressure from patches on the panel, where 50% or more of the patch is on the panel or, for coarser discretizations, the pressure of the patch that covers the panel.

Figure 22 shows a selection of differently patched cones. The inverse problem is solved for varying numbers of patches to understand the impact of this discretization. The Tikhonov scaling is 10^{-5}. The patches are decreased in size in a manner that maintains a consistent patch aspect ratio. The mean predicted panel pressure autospectrums for varying numbers of patches are shown in Figure 23. For small numbers of patches the autospectrum is similar to that of the experiment while for larger numbers of patches the predicted pressure is larger than the measured value. In these figures the mean autospectrum of pressure as measured in the experiments is shown via a model that was directly fitted to the wind tunnel data.

Table 2 shows the total run time for the inverse problem using 2 nodes and 16 processes on each core on a cluster with two Intel SandyBridge EP CPUs per node, each CPU having 8 cores. The number of patches on the panel (if more than one, the number with more than 50% of the patch on the panel) is also shown and demonstrates how many total patches are needed to begin to well discretize the panel and additionally it shows the inconsistency in the total number of patches and the actual number covering the panel. Figure 24 shows the autospectrum of the acceleration response for varying pressure discretizations. The measurement DOF that has the largest magnitude of response is usually well matched no matter the discretization while agreement across all DOFs only occurs when there is a finer discretization. The number of matched DOFs does appear to match the number of patches that lie on the panel. One might expect that patches that do not lie on the panel should still be able to excite panel modes via the boundaries; though the magnitudes would be larger so they would be more sensitive to Tikhonov scaling. The authors were unable to demonstrate better fits with few panel patches even with no Tikhonov regularization. It is not clear whether this is due to the optimization solver settings or some other phenomena.

The impact of boundary condition on the sting can also be studied using the inverse problem. For results shown previously in this section, the sting is fixed in place and the response at G2 (near the sting) is ignored in the inverse

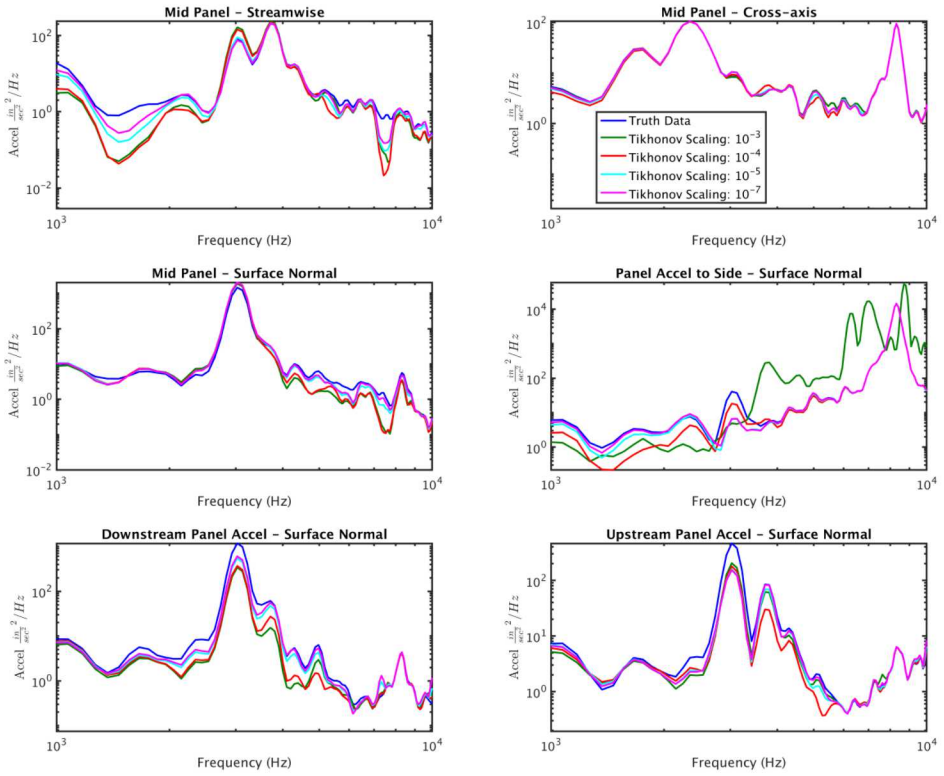

Fig. 19 Depiction of varying Tikhonov scaling on wind tunnel data match using 45 patches.

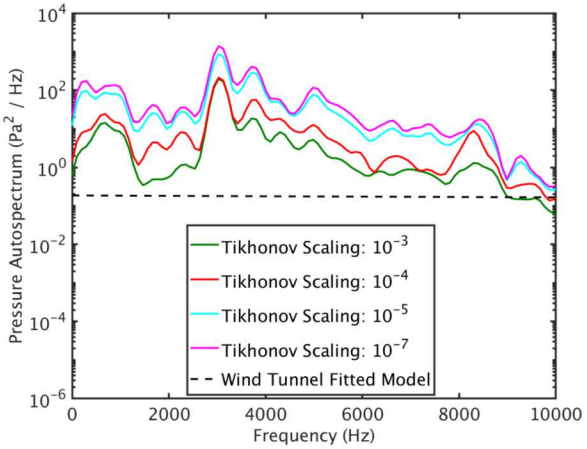

Fig. 20 Predicted mean patch pressure loads with varying Tikhonov scaling.

problem. The Mach 8, composite panel configuration was specifically chosen as it was determined that the motion of the sting had the least impact on the panel response. The boundary condition could be included in the fit in a number of ways: pre-processing the data and using the model to remove the response due to the sting motion, by prescribing the sting motion directly or by solving for the forces at the sting as part of the inverse problem. Due to limitations in how accelerations can be prescribed in Sierra/SD for modal methods it was chosen to directly solve for forces on the

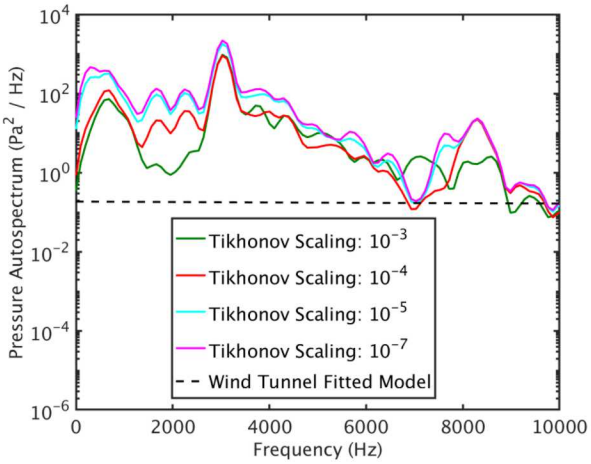

Fig. 21 Predicted mean panel patch pressure loads with varying Tikhonov scaling.

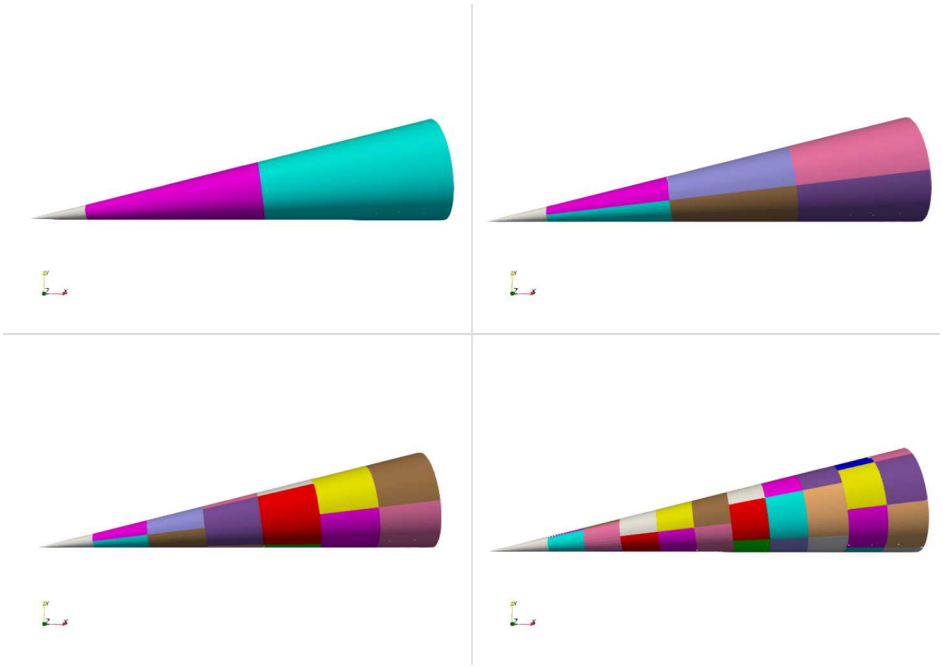

Fig. 22 Depiction of varying patch discretizations on cone.

sting in addition to the patch pressures in a single inverse problem while matching the response at all accelerometers (G1,G2,G3,G4 and G5).

Figure 25 shows the comparison of predicted pressures resulting from the inclusion or exclusion of the G2 response and sting forces. Here the Tikhonov scaling is 10^{-7} and a mesh with 21 patches is used. For the entire frequency range, the predicted pressures when matching sting motion are smaller than those where the sting is considered fixed. The largest differences are seen at frequencies below 2kHz. The comparison of response with different boundary conditions is shown in Figure 26. Visually the responses when using different boundary conditions are very similar except on the body accelerometer (G2) and at a handful of distinct frequency and measurement DOF combinations. These comparisons are visually similar to those in which G3 is also part of the inverse problem.

The inclusion of the sting forces and G2 in the inverse problem is complicated by the Tikhonov regularization. The Tikhonov regularization treats the time histories of all unknown forces and pressures as a single vector of variables, which is accumulated and then scaled. The TBL pressures are expected to be relatively constant in their RMS from

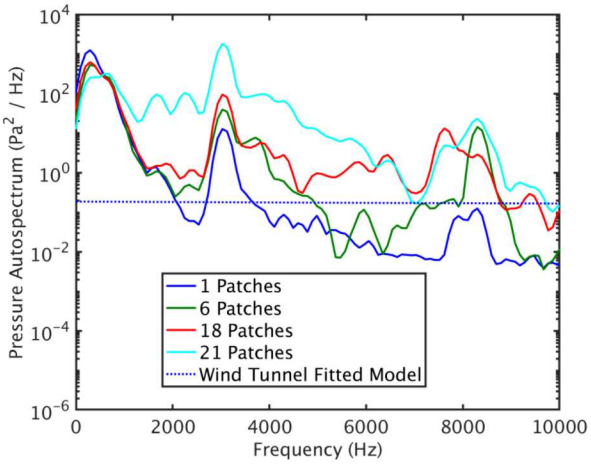

Fig. 23 Predicted pressure loads with varying number of patches on body.

Table 2 Total Run Time for Time Domain Inverse Problem with 4 Iterations.

Number of Patches	Computational Time (hr:min)	Number of Patches on Panel
1	3:11	1
6	6:34	1
18	14:41	2
21	16:53	4

patch to patch, so there is no need to scale patches differently. The sting forces are fundamentally different than the TBL pressures however and are expected to have different scaling, so the application of a naive Tikhonov may have different impact on the different loads. In the model a concentrated mass with mass of 10^4 lbm is connected to the cross section of the sting and is where the forces are applied.

Given the predicted and measured TBL pressures with fixed sting, the magnitude of the concentrated mass, and the magnitude of the accelerations at G2, an estimation of scalings can be made for the sting forces. A sensible scaling would be 10^4 to generate similarly scaled sting force unknowns and pressure unknowns if the expected pressures were of magnitude one and the accelerations at G2 were of magnitude one times gravity. In Figure 27 the predicted pressures are shown with both differing Tikhonov scalings and sting force scalings; the resulting pressure predictions vary drastically in magnitude with scaling. The sting force scales vary from 10^4, where the sting force unknowns will be large relative to the TBL pressures, to 10^8, where the sting force unknowns should be small relative to the TBL pressure unknowns. Figure 28 shows the predicted response when using varying Tikhonov and sting force scalings. The relationship between the scalings and the relative match is not obvious, Table 3 showing the quantitative L2 error measures. The one clear and expected result is that a small sting scaling coupled with a relatively large Tikhonov scaling will result in poor agreement at G2.

Table 3 Response agreement for varying Tikhonov and Sting Force Scalings.

Tikhonov Scaling	Sting Force Scaling	L2 Relative Error
10^{-3}	10^4	0.01781
10^{-7}	10^4	0.005092
10^{-3}	10^6	0.01181
10^{-3}	10^8	0.02146

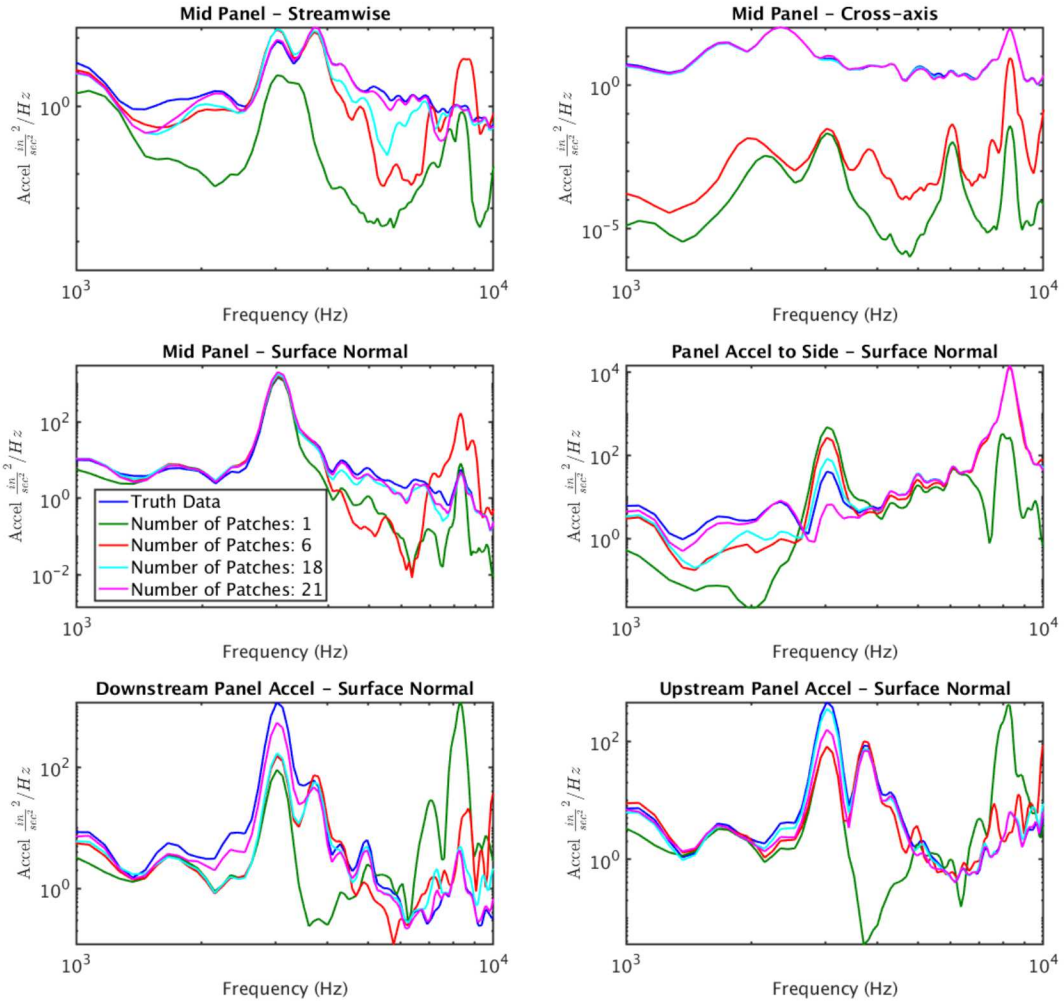

Fig. 24 Predicted response with varying number of patches on body.

VII. Discussion

There are a number of conclusions that can be drawn from this study. Constructing and verifying a MATLAB® implementation of the frequency domain representation of a complicated TBL pressure model along with all the machinery to handle arbitrary cone meshes and FE model details was time consuming. Constructing and verifying the machinery to take experimental data, FE models and construct the inverse problems for various parameter studies was also time consuming.

Over the course of the study it was noted that varying model and parameter choices in the frequency domain approach had less impact on the predicted pressure autospectrums than varying model and parameter choices in the time domain. This is logical as the frequency domain method was constructed so that unique solutions could be generated. The problem was regularized by enforcing parts of the pressure model that had previously been derived. The time domain methods in Sierra/SD utilized regularization that was not tailored to the problem and effectively penalized the quantity of interest, the pressure autospectrum.

There are a number of improvements to this work that could be studied in the future specifically to address the complications identified in this work, such as reimplementing the frequency domain method in a more computationally efficient manner and incorporating more physics specific regularization into the time-domain Sierra/SD methods. At

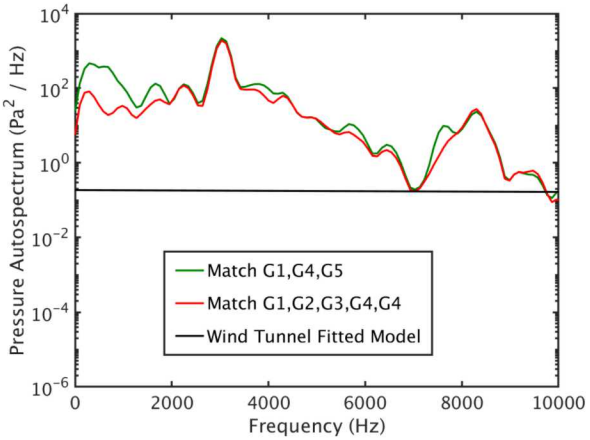

Fig. 25 Comparison of mean predicted panel pressure loads when using fixed boundary condition or not.

present the time-domain problem is quadratic, so a second order optimization scheme should be able to solve it well and quickly given the addition of appropriate preconditioning. The frequency domain problem as constructed was nonlinear due to the details of the TBL models used and parameter choice. Implementing more physics specific regularization to the Sierra/SD time-domain scheme would likely drive that problem to have some more complicated nonlinear form as well. While the optimizations methods available in Sierra/SD should be sufficient for this task the cost of implementing the regularization scheme should be considered. Particularly the regularizations that are physics specific may continue to change form as the TBL pressure models are refined.

Re-implementation of the frequency domain approach in a format that would provide for more computational efficiency can also be considered, such as C++ with care taken to provide good parallel performance. Improvements to this scheme should also be carefully considered given that it relies on a linear structural dynamics model of the system and an assumption of stationary pressure loading.

Looking forward to the broader application of these techniques to problems such as typical fixed-wing aircraft there are a number of additional complexities to be considered. Phenomena such as gusts or laminar-turbulent transition may not be well described as stationary processes. For larger loads, nonlinearities in the structure may become important to the vehicle response. More complicated geometries will also require more complicated models of fluid loading, which may become cumbersome. To the authors it seems that there is no single solution to these problems. For short studies where the loading is expected to be of a certain form and little detail is known about the structure, techniques such as the frequency domain scheme shown here are likely best. Reasonable estimates of pressure loading were achieved with little effort once the framework was developed and there was much less care needed in studying the impact of discretization and parameter choice. There will be more complicated problems where additional physics are important, however, the maturation of frameworks in Sierra/SD or similar tools is necessary to provide ever more complicated representations of the loading phenomena, with parameterization, regularization, and implementation (ex. need of gradients) choices that are problem specific. Reduced order modeling techniques for representing the structural dynamics should also be considered a key component of these inverse problems as they will have significant impact on the computational cost of the overall problem.

VIII. Conclusions

The frequency domain approach with a tailored TBL pressure loading model was demonstrated and found to be an effective, computationally efficient approach to this problem. It is inherently limited to problems where the primary loading is due to pressure fluctuations in the turbulent boundary layer, that pressure is stationary and the structural dynamics are linear. Problems involving laminar or transitional flow, or that are simply non-stationary will be poorly represented by this approach. Very generic time domain methods suffer from ill-posedness, having a limited set of data relative to the complexity of pressure to be identified and rely on regularization that can be problematic. With careful study the complexities of the modeling and regularization choices can be understood and good representations of pressure loading generated. In the future more physics driven regularizations should be studied for the time domain

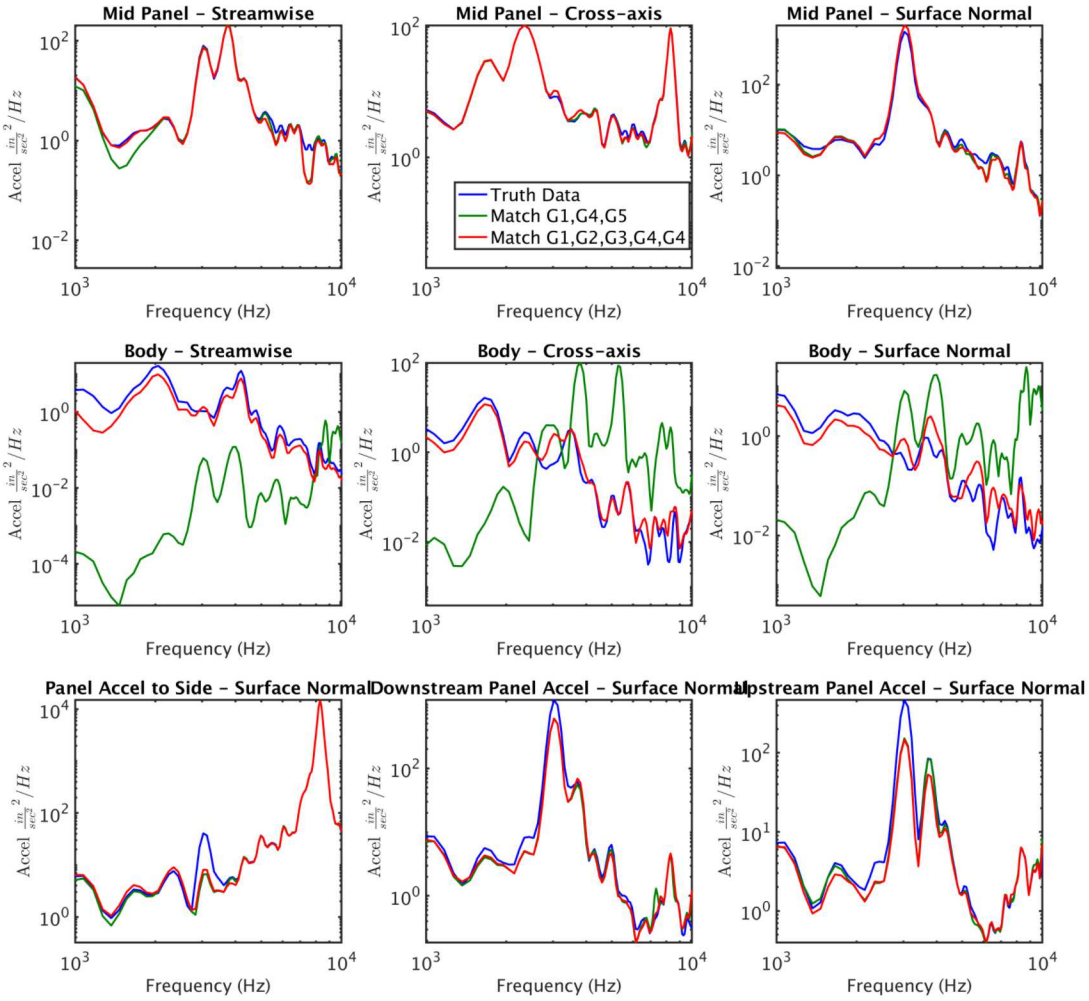

Fig. 26 Comparison of predicted response when using fixed boundary condition or not.

scheme and for further validation, comparisons should be made at sensor locations not included in the inverse problems.

Acknowledgments

The authors thank numerous colleagues for their contributions that made this work possible. Mikhail Mesh performed test planning and model development that this work was built upon. Jerry Rouse provided guidance for method development, particularly in the frequency domain. Katya Casper performed the critical experiment that is used for validation and comparison. Patrick Hunter performed structural hammer tests of the experimental model. Brian A. Robbins remains a constant collaborator in the modeling of this experiment. Tim Walsh led development for the inverse methods capabilities utilized in Sierra/SD. Richard Bradley performed initial studies on using Sierra/SD's force identification capability for this problem. Finally, Larry Dechant provided guidance regarding models of turbulent boundary layer pressure.

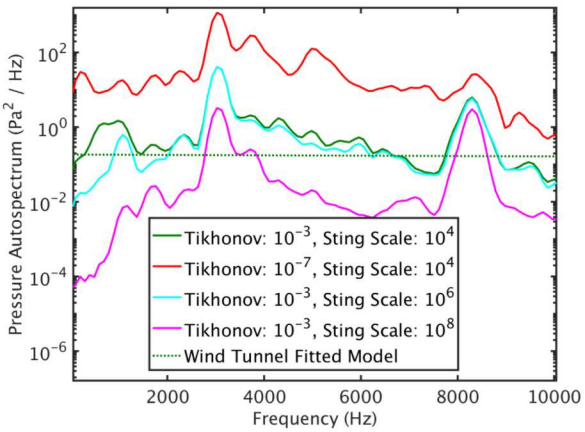

Fig. 27 Mean predicted panel pressure loads when matching response on G2 and varying scalings.

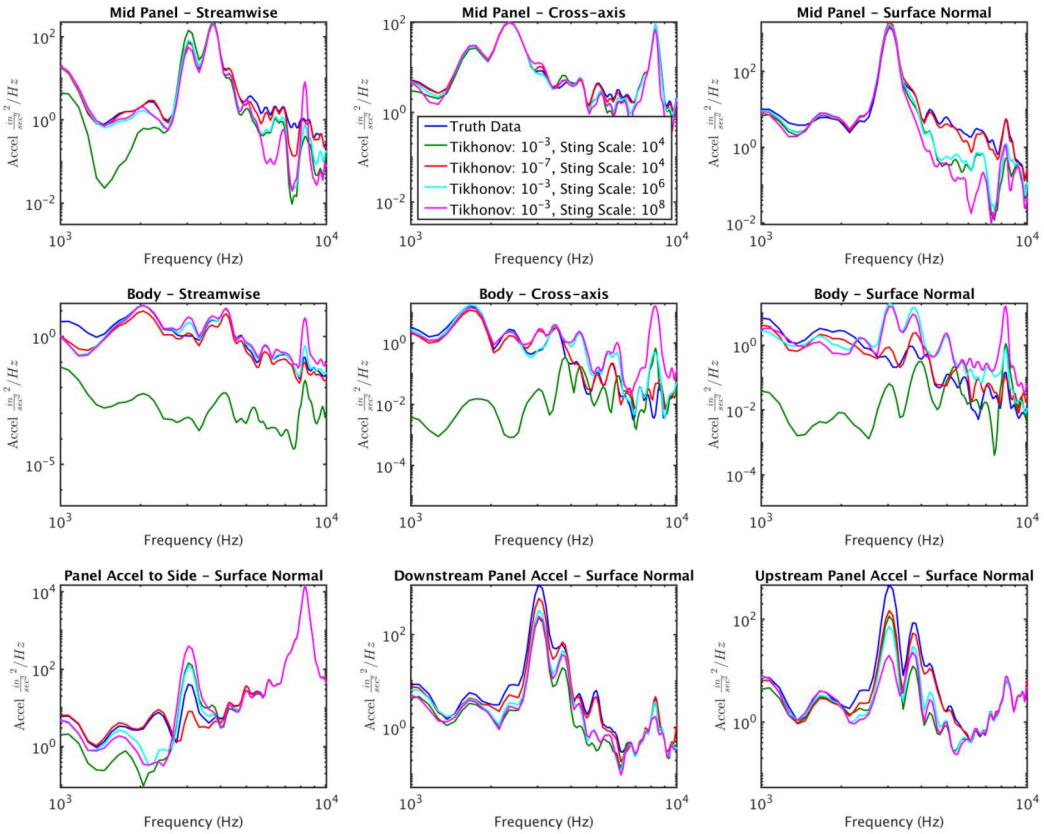

Fig. 28 Predicted response when matching response on G2 and varying scalings.

References

[1] Larmat, C., Tromp, J., Liu, Q., and Montagner, J.-P., "Time reversal location of glacial earthquakes," *Journal of Geophysical Research: Solid Earth*, Vol. 113, No. B9, 2008.

[2] Kawakatsu, H., and Montagner, J.-P., "Time-reversal seismic-source imaging and moment-tensor inversion," *Geophysical Journal International*, Vol. 175, No. 2, 2008, pp. 686–688.

[3] Unnthorsson, R., Runarsson, T. P., and Jonsson, M. T., "Acoustic emission based fatigue failure criterion for CFRP," *International Journal of Fatigue*, Vol. 30, No. 1, 2008, pp. 11–20.

[4] Carpinteri, A., Lacidogna, G., and Pugno, N., "Structural damage diagnosis and life-time assessment by acoustic emission monitoring," *Engineering Fracture Mechanics*, Vol. 74, No. 1-2, 2007, pp. 273–289.

[5] Kouri, D. P., Heinkenschloss, M., Ridzal, D., and van Bloemen Waanders, B. G., "A trust-region algorithm with adaptive stochastic collocation for PDE optimization under uncertainty," *SIAM Journal on Scientific Computing*, Vol. 35, No. 4, 2013, pp. A1847–A1879.

[6] Jeong, C., Peixoto, A. C. S., Aquino, A., Lloyd, S., and Arhin, S., "Genetic Algorithm–Based Acoustic-Source Inversion Approach to Detect Multiple Moving Wave Sources of an Arbitrary Number," *Journal of Computing in Civil Engineering*, Vol. 31, No. 5, 2017, p. 04017020. doi:10.1061/(ASCE)CP.1943-5487.0000664.

[7] Aguilo, M. A., Aquino, W., Brigham, J. C., and Fatemi, M., "An Inverse Problem Approach for Elasticity Imaging through Vibroacoustics," *IEEE Transactions on Medical Imaging*, Vol. 29, No. 4, 2010, pp. 1012–1021. doi:10.1109/TMI.2009.2039225.

[8] Kim, K., Fee, D., Yokoo, A., and Lees, J. M., "Acoustic source inversion to estimate volume flux from volcanic explosions," *Geophysical Research Letters*, Vol. 42, No. 13, 2015, pp. 5243–5249. doi:10.1002/2015GL064466, URL https://agupubs.onlinelibrary.wiley.com/doi/abs/10.1002/2015GL064466.

[9] Taroudakis, M. I., and Makrakis, G., *Inverse problems in underwater acoustics*, Springer Science & Business Media, 2013.

[10] Walsh, T., Aquino, W., and Ross, M., "Source Identification in Acoustics and Structural Mechanics using SIERRA/SD," *Sandia National Laboratories SAND Report*, 2013.

[11] Smith, J. A., DeChant, L. J., Casper, K. M., Mesh, M., and Field, R. V., "Comparison of a Turbulent Boundary Layer Pressure Fluctuation Model to Hypersonic Cone Measurements," *34th AIAA Applied Aerodynamics Conference*, AIAA, 2016. doi:10.2514/6.2016-4047, URL https://arc.aiaa.org/doi/abs/10.2514/6.2016-4047.

[12] Corcos, G., "Resolution of pressure in turbulence," *The Journal of the Acoustical Society of America*, Vol. 35, No. 2, 1963, pp. 192–199.

[13] Casper, K. M., Beresh, S. J., Henfling, J. F., Spillers, R. W., Hunter, P., and Spitzer, S., "Hypersonic Fluid–Structure Interactions Due to Intermittent Turbulent Spots on a Slender Cone," *AIAA Journal*, Vol. 57, No. 2, 2019, pp. 749–759. doi:10.2514/1.J057374, URL https://doi.org/10.2514/1.J057374.

[14] Wirsching, P. H., Paez, T. L., and Ortiz, K., *Random vibrations: theory and practice*, Courier Corporation, 2006.

[15] Bunting, G., Crane, N. K., Day, D. M., Dohrmann, C. R., Ferri, B. A., Flicek, R. C., Hardesty, S., Lindsay, P., Miller, S. T., Munday, L. B., et al., "Sierra Structural Dynamics-Users Notes 4.50." Tech. rep., Sandia National Lab.(SNL-NM), Albuquerque, NM (United States), 2018.